New droplet aero-breakup mechanism associated to unsteady flow loading

A. García-Magariño[1], S. Sor[1], A. Velazquez[2*]

[1]National Institute of Aerospace Technology (INTA), 28850, Madrid, Spain

[2] Fluid Mechanics and Aerospace Propulsion Department. Technical University of Madrid, Plaza del Cardenal Cisneros 3, 28040 Madrid, Spain

Abstract

Experimental testing on the unsteady aero-breakup of ethyl alcohol droplets was carried out at the rotating arm facility of INTA. The selection of the working fluid was driven by the need to explore wider ranges of the dimensionless parameters that govern the problem. A model airfoil was attached at the end of a 2.3 m long rotating arm driven by an electric motor. Droplets, whose diameter ranged from 500 μm to 1500 μm, were allow to fall in the path of the airfoil that attained velocities in the range between 30 m/s and 60 m/s. Droplets trajectories and breakup modes were recorded, and a new breakup mode was identified. Its sequence is as follows: 1) the droplet deforms as an oblate spheroid, 2) a bulge appears and grows on its flow facing surface, 3) the droplet thickens in the stream-wise direction; 4) the thickening in the rear part of the droplet develops in the shape of a cone, 5) the cone grows thinner until a finger like shape is formed. Additionally, based on a theoretical model developed by the authors, a

comparison has been made between the deformation and breakup onset phases of ethyl-alcohol and water droplets up to the instant of breakup.

[*] **Corresponding author:** angel.velazquez@upm.es, 00 34 91 0675792

1. Introduction

The study of droplet breakup mechanisms is a prolific area of research and development. A quick search in the Web of Science (Clarivate Analytics) shows about 600 entries on the subject during the past 20 years, most of them Journal articles. The reason could be that the dynamics of droplet breakup involves many fundamental Fluid Mechanics issues as well as a large variety of practical industrial applications. In this context, two time periods could be broadly described when looking at the specialised literature. The first one is about understanding and systematizing droplet breakup processes, while the second is concerned with applications of increasing levels of complexity. To have a broad overview of the first, the reader is directed towards three key reviews. Chronologically, they are those of Pilch and Erdman [1], Guildenbecher et al [2], and Theofanous [3].

The work of Pilch and Erdman [1], published in 1987, has been the inspiration for many subsequent studies. The authors considered the problem of a constant speed airflow past a liquid droplet. The airflow causes the liquid droplet to attain

an accelerated motion which leads, in turn, to the generation and ulterior growth of surface instabilities (Taylor waves) that may cause droplet breakup. The authors characterised the incoming airflow using the Weber number, $We = \rho V^2 D / \sigma$, where ρ and V are the air density and constant velocity, and D and σ are the droplet diameter and surface tension respectively. Five breakup mechanisms were identified by the authors: 1) $We \leq 12$: vibrational; 2) $12 < We \leq 50$: bag; 3) $50 < We \leq 100$: bag-and-stamen; 4) $100 < We \leq 350$: sheet stripping; and 5) $350 < We$: wave crest stripping followed by catastrophic breakup. An explanatory sketch of each breakup mechanism was presented in table 1 of said ref. [1]. It is interesting to note that the authors devoted a whole sub-section to the issue of the "Initiation of breakup" (subsection 2.3.1 of ref. [1]) where they explicitly wrote: *"The definition for initiation of breakup is somewhat arbitrary, and the definition varies according to the breakup mechanism"*. 33 years later, the authors of the present study still agree with this statement delivered in ref. [1]. Also, it is worth highlighting that this study of Pilch and Erdman [1] addresses the situation of a constant airflow velocity only. Then, some questions that remain are: a) what happens when the incoming flow has an unsteady nature? i.e.: does unsteadiness in the incoming flow affect the breakup mechanism? And b) what are the dimensionless parameters that govern the problem in this unsteady state situation?

Guildenbecher et al [2] started their article with a detailed discussion on the pros and cons of the three most common types of experimental facilities used for these studies; namely: shock tubes, continuous jets, and drop towers. Next, the authors described the breakup mechanisms and, apart from some nomenclature aspects,

they reported the same five categories of Pilch and Erdman [1]. Then, the authors went on describing in detail the different stages and physical phenomena associated to the five breakup mechanisms. They did it accounting for the new wealth of experimental and numerical evidence that was generated during the 22 years that elapsed between publication of references [1] and [2]. The authors also discussed and compared different models to predict droplet deformation and breakup phases; and reviewed in detail the issue of non-Newtonian fluids. Again, this review article focussed on the case of a constant velocity airflow; being either of a step-like nature in shock tube facilities, or nearly constant in continuous jet experimental rigs.

The work of Theofanous [3] is interesting because the author aimed to unify the different droplet breakup mechanisms observed up to its publication date (2011) into just two different modes. The key ingredient for this unification attempt was the study of the competition between Rayleigh-Taylor and Kelvin-Helmholtz instabilities in the frame of prescribed Fluid Mechanics (Aerodynamics) conditions. Two main regimes were described (the author calls them: "patterns of bodily loss of coherence") that can be broadly identified as either the case in which the airflow penetrates, at some stage, the droplet, or the case when the airflow goes around the droplet. In practical terms, these two regimens were named as "Rayleigh-Taylor piercing, RTP" and "shear induced entrainment, SIE". In a sense, RTP encompasses the vibrational, bag and bag-and-stamen regimes of references [1-2], and SIE encompasses the sheet stripping and catastrophic breakup. The 42 references included in this study were analysed in view of the proposed unifying theory which provides the reader with a rather broad overview

of the field. As in the previous references, most of the cases discussed here referred to the situation of a constant velocity incoming flow. Complementarily, the reader interested in the details of the Raileigh-Taylor instability theory that lies at the heart of the findings presented in ref. [3] is directed to the article of Krechetnicov [4].

Once the generic frame of droplet aero-breakup was, more or less, stablished, a trend could be identified in the specialised literature that relates to the study of specific, very sophisticated, application cases that do not necessarily fit into the general framework reviewed so far. This is not because the physics is different, but because the conditions are different. Recall that conditions addressed in refs. [1-4] were constant velocity and isothermal airflow past initially perfect liquid droplets (they will be called "canonical conditions" for the remainder of the article). For example, very recently, Chaitanya and Saptarshi [5] have studied the breakup mechanism of a levitated evaporating (under external heating) emulsion droplet. The authors observed three regimes during the process: droplet deformation, vapor bubble nucleation, and high intensity breakup in the shape of a crown-like sheet different from the forms observed in refs. [1-4]. Ashar et al [6] have reported on the breakup of droplets placed inside rotor-stator mixers. The authors found that under these highly confined conditions, primary droplets tended to break into clouds of smaller secondary droplets. The number of these secondary droplets varied between two and fourteen. One of the interesting conclusions, contrary to what has been observed in other studies, was that the probability of achieving binary breakup was smaller than that of having multiple breakup. Piskunov and Strizhak [7] studied the catastrophic disintegration of water slurry droplets in

boiling conditions. An interesting study on a slight variation of the canonical conditions has been reported by Kumar et al [8]. The authors allowed water and water-glycerine droplets to free-fall while immersed on an oblique airstream. Glycerine to water ratios varied between 50 % to 80 % and the angle of inclination varied between 0 deg (normal to the free-fall path) and 60 deg. Then, this study addressed conditions in which gravity forces were at an acute angle with regard to the direction of the incoming velocity. The breakup modes considered were vibrational, bag, and the transition between them. The main conclusion of the study was that the critical Weber number (flow velocity was constant) that defines transition between breakup modes is rather sensitive to the variation on droplet topology caused by the skewed airstream. That is: the authors still reported the canonical breakup modes but transition between them was found to be critically dependent of the governing flow parameters. Breakup of droplets of coal water slurries has been studied experimentally by Zhao et al [9] and numerically by Minakova et [10]. The complexity of this breakup mechanism can be appreciated in figures 2, 3, 4, and 5 of ref. [10] where a comparison is presented between experimental and numerical results. It is remarkable that, in some cases, an external torus of fluid can be perfectly identified while the interior undergoes an explosive breakup. Droplet breakup in the highly confined conditions of a flow focusing device has been studied by Pan et al [11]. The authors established that the neck breakup dynamics proceed along two stages: squeezing and fast pinch-off. An experimental study on droplet deformation and breakup in an oblique air-stream has been performed by Soni et al [12]. This type of configuration occurs in gas turbine combustors and the authors obtained the values of the critical Weber number as a function of the Eötvös number, the air stream inclination

angle, and the Ohnesorge number for the bag type breakup mode. Finally, although they address the canonical breakup mechanisms, it is worth referencing the work of Strotos et al [13] because they describe in detail a CFD approach to the problem, and numerically simulate and compare with experiments two cases belonging to the RTP and SIE limits described above. Also, although it is not a review article itself, the authors deliver a comprehensive and useful introduction section that generalizes and classifies previous results (the article contains 50 references).

A different class of breakup modes is the one associated to unsteady incoming flows. For instance, unsteady flows appear (in the droplet reference frame) when a blunt body approaches the droplet at constant velocity. The nature of the potential flow solution in the stagnation streamline (in the blunt body reference frame) is of the form: $U \sim r^{-n}$, where U , r, and n are velocity in the stagnation streamline, distance to the body, and a geometry related coefficient respectively. For example, in the case of a circular cylinder $n = -2$ and $U = U_\infty \left[1 - (r/R)^{-2}\right]$, where U_∞ and R are velocity at infinity and body radius respectively. When this expression for U is transposed to the droplet reference frame, the velocity of the flow past the droplet, U_{slip} , scales as $U_{slip} \sim [d(t)]^{-n}$ where $d(t)$ is the time dependent distance from the droplet to the incoming blunt body. In this case, the velocity U_{slip}, and all its derivatives increase monotonously, see Section 4 below, equations (5-6), and the associated explanation. The situation just described appears, for example, in aeronautics related flows when the motion of a lifting/control surface (a wing or a rudder) through rain is considered. The specific problem of droplet deformation and breakup under unsteady flow conditions has

been addressed by Garcia Magariño et al [14]. The authors used a rotating arm experimental facility in which a stream of droplets was allowed to fall into the path of an airfoil placed at the end of a rotating arm. The two main conclusions of the study were that the bag-and-stamen breakup mechanism exists in unsteady conditions, also, and that the onset of breakup is anticipated as compared to the case of steady flows. In Garcia Magariño et al [15] the authors were able to generalize the results by using a High Order Singular Value Decomposition approach applied to the time dependent data bases obtained. Sor et al [16] developed a theoretical model for the deformation and trajectory of droplets in these transient conditions. They proposed a new formulation for the droplet unsteady drag term (that affects both trajectory and deformation) and the theoretical predictions obtained with the model yielded a reasonable agreement with experimental data. Finally, Lopez-Gavilán et al [17] coupled the droplet deformation model to a breakup model based on tracking the growth of droplet surface Taylor waves that led to instability and ulterior breakup. Also, a related study has been presented by Veras-Alba et al [18] but, in this case, the falling droplets were super-cooled.

At this point, the question was: does the presence of unsteady flow involve new breakup mechanisms, or does it merely change the parametric thresholds between the canonical ones? On one hand, the experimental studies presented in references [15] and [17-18] did not find new mechanisms. On the other, the theoretical models presented in [17-18] involved the presence of dimensionless governing parameters that were explored in a limited range only. Then, the objective of the present work is to expand that parametric range to answer the

question of whether unsteady conditions may lead, or not, to new mechanisms of droplet breakup. To this end, geometric and operational parameters, as well as the working fluid, were changed in the experiments.

As for the organization of the work, the experimental setup is described in section 2. Results are presented and discussed in sections 3 and 4 respectively; and the conclusions are summarized in section 5.

2. Description of the experimental setup

The unsteady flow field in the reference frame of the droplets was generated by using the rotating arm facility of INTA, see ref. [14] for more details. An overview of this facility is presented in the two pictures, left and right, of fig. 1.
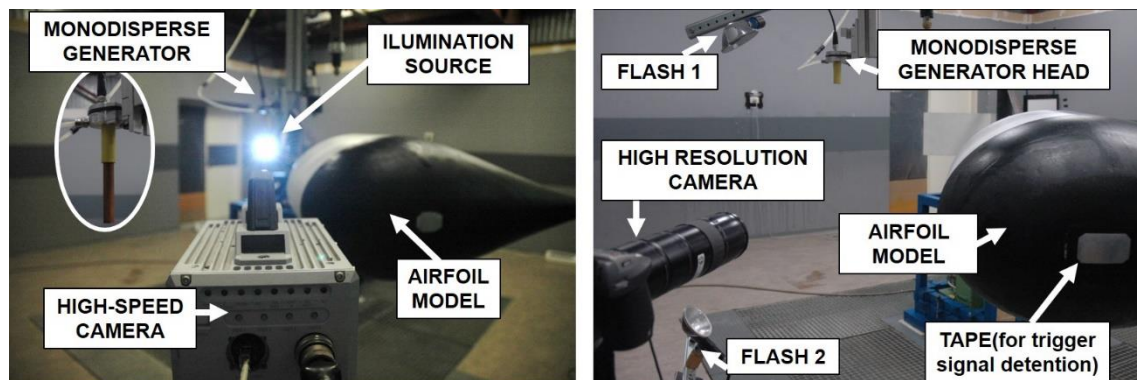
Figure 1. Two views of the experimental facility and its main data acquisition systems

The facility consists of a rotating arm (length equal to 2.16 m) attached to the axis of an electric motor (power equal to 5 kW). The axis was pointing in the vertical direction, so the rotating arm moved in a horizontal plane. A blunt airfoil model

were placed at the end of the arm. Streams of droplets were allowed to fall on path of the incoming airfoil so that the air flow in the droplets reference frame was characterised by a monotonically increasing velocity and higher order derivatives. One of the limitations of the study, as indicated in the Introduction section and described in more detail in the Discussion section, see equation (6), is that $U_{slip} \sim [d(t)]^{-n}$ in the present rotating arm experimental facility. Furthermore, if the rotating arm moves at constant velocity, it happens that: $U_{slip} \sim [U_m t]^{-n}$. This means that the conclusions of this study can be applied to potential type of unsteady aerodynamics loading only. The way to prescribe more generic laws of aerodynamic loading would possibly be to implement a control system in the rotating arm that changes its rotational velocity within each cycle. This could be a promising line of research, but it is out of the scope of the present work. Given the drag of the airfoil model, the maximum rotational velocity of the arm was 250 rpm that translates into an airfoil velocity of 60 m/s. The monosized droplet generator was developed in-house and used ethyl alcohol as the working fluid (density and surface tension equal to 789 kg/m^3 and 0.023 N/m respectively).

Two experimental campaigns were conducted using two different acquisition systems to obtain both qualitative and quantitative results. First (see fig. 1 left), images were recorded using a PHOTRON SA4 high speed camera. The optical lenses were AF Micro Nikkor 200mm 1:4D. The acquisition rate, AR, was varied between 30,000 and 45,000 frames per second, fps. The actual selection of fps depended on droplet diameter, D, and resolution, Rs, see table 1. During this first experimental campaign, a 3W LED system was used to back-illuminate the droplets. Shadowgraph images were generated in this way, and quantitative

datasets were obtained to analyse the breakup onset. For instance, the evolution of the droplet maximum and minimum diameters during the deformation phase was measured and used to define the time of breakup onset. During the breakup phase itself, the high acquisition rate of the shadowgraph images allowed for a detailed observation the evolution of the breakup topology.

D (µm)	Rs. (pix)	AR. (fps)
500	256 x 285	40,000
1000	192 x 304	45,000
1500	192 x 480	30,000

Table 1. Optics experimental conditions, resolution in pixels (RS) and acquisition rate (AR), as a function of droplet diameter (D).

Second, to obtain higher resolution images at specific time instants during the breakup phase, a second experimental campaign was conducted with a higher resolution camera. In this second campaign, instead of shadowgraph images, a direct illumination was used to collect qualitative data of the breakup topology. The illumination system in the second experimental campaign can be observed in fig. 1 right. Two flash lamps, the 1538-A Strobotac Electronic Stroboscopic and the 1539-A Stroboslave, illuminated the droplets. Duration of the flash was about 3 µs. Images were collected by using a high-resolution Hasselblad H3DII-39 camera. Its resolution was 7216 x 5412 pixels (width by height). The magnification was 151 pix/mm. The lenses were HC 4/200 mm, with two extensions H52 mm, and a converter H1.7x. The camera setup was ISO-800 and f/6.8. A LED trigger was located close to the airfoil trajectory to detect a piece of

tape glued to the model side as it followed its circular path (see fig. 1). The flashes and the trigger signal were delayed by a certain time lag using a Programmable Timing Control Hub IDT. Control of this time lag allowed to vary the distance between the droplets and the model.

The airfoil model, tagged as DBK004, had a chord, C, of 1.05 m, and a leading edge radius, Rc, of 0.157 m. Its dimensionless coordinates are given in table 2. A view of the model can be seen in fig. 2.

X/C	Y/C	X/C	Y/C
1.000	0.000	0.241	0.200
0.937	0.014	0.211	0.196
0.877	0.028	0.183	0.191
0.818	0.044	0.157	0.183
0.762	0.059	0.133	0.173
0.707	0.076	0.110	0.162
0.655	0.093	0.090	0.150
0.604	0.110	0.072	0.136
0.556	0.127	0.056	0.121
0.510	0.143	0.042	0.105
0.465	0.158	0.030	0.089
0.423	0.171	0.020	0.072
0.383	0.183	0.012	0.055
0.344	0.192	0.006	0.041
0.308	0.198	0.002	0.022
0.274	0.200	0.000	0.000

Table 2. Dimensionless coordinates, X/C and Y/C of the selected airfoil.
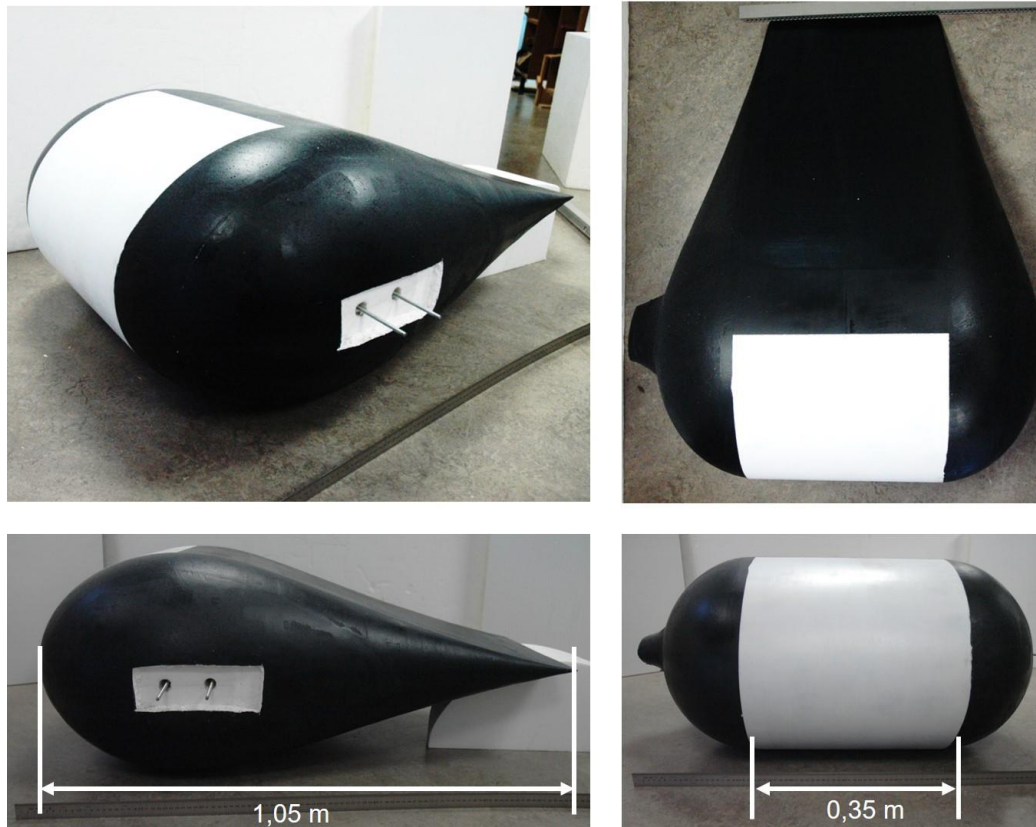
Figure 2. Four views of the airfoil model including its main dimensions in m.

The velocity of the model in the experiments was varied in the range from 30 m/s up to 60 m/s. The air velocity profiles and accelerations, as viewed from the droplet reference frame, are presented in fig. 3 for four different model velocities: 30 m/s, 40 m/s, 50 m/s, and 60 m/s respectively. In these cases, the initial distance from the droplets to the model was 0.5 m. These velocity profiles were obtained by using a Particle Image Velocimetry, PIV, setup. The working details of this system are given in ref. [14] and are omitted here for the sake of brevity.
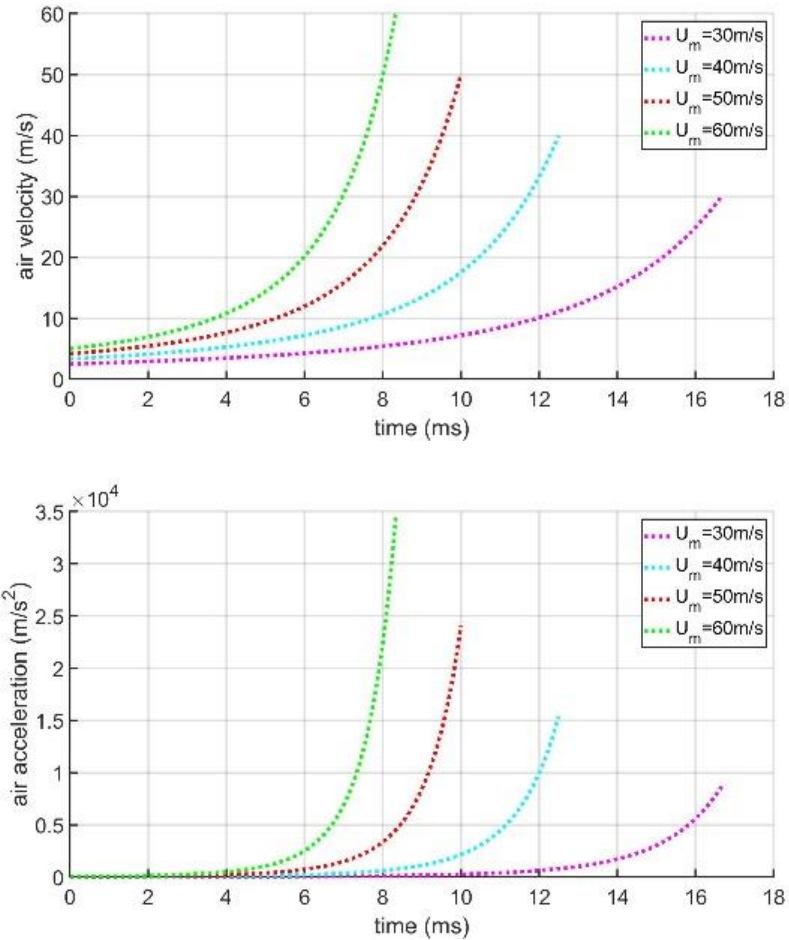
Figure 3. Flow velocity and acceleration time profiles in the droplet reference frame for four different constant velocities (30 m/s, 40, m/s, 50 m/s, and 60 m/s) of the airfoil model.

Next, the issue of flow uniformity around the droplets is addressed. Fig. 4 presents three PIV measured horizontal air velocity profiles located at: a) the airfoil stagnation streamline, and b) above and below said stagnation line at distances of ± 12 mm. It could be observed that the three velocity profiles basically collapse into one. This implies that within a band of 24 mm centered around the stagnation streamline (that is larger than the typical droplet diameter ~ 1 mm) the flow around the droplet could be considered as uniform. Note that the abscissa represents the distance from the reference frame of the droplet to

the incoming airfoil. The origin of this reference is located at the point where the airfoil is 510 mm away from the droplet.
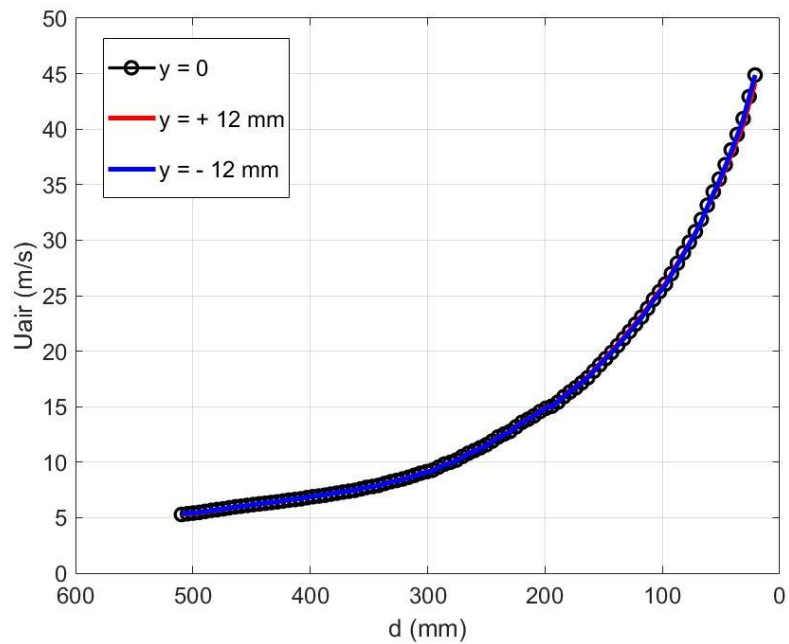
Figure 4. PIV measured air velocity profiles at the incoming airfoil stagnation region as a function of the distance between droplet and airfoil. Black line with circle marks: stagnation streamline, red line: 12 mm above the stagnation streamline, blue line: 12 mm below the stagnation streamline.

3. Results

3.1. Matrix of experimental cases

Twelve different cases were considered. They corresponded to four model velocities: 30 m/s, 40 m/s, 50 m/s, and 60 m/s, and three droplet diameters: D = 500 μm, D =1000 μm and D =1500 μm. Table 3 shows the case key for each of the cases

Each case was experimentally tested several times. The behaviour of the different droplets within each case was similar (the issue of repeatability is addressed in Annex 1). In the sub-sections that follow, only one droplet sequence per case is described.

Case Key #	D = 500 µm	D = 1000 µm	D = 1500 µm
U_m = 30 m/s	1	5	9
U_m = 40 m/s	2	6	10
U_m = 50 m/s	3	7	11
U_m = 60 m/s	4	8	12

Table 3. Key of the experimental cases.

The rationale behind the selection of these cases is related to the characteristics of the experimental facility, and, also, to physical modelling considerations. It has been found that when either water or alcohol droplets are considered (surface tension equal to 0.073 N/m and 0.023 N/m respectively) the unsteady flow loading provided by INTA's rotating arm facility is not able to break droplets whose diameter is smaller than about 500 µm. In these cases, surface tension effects dominate the droplet deformation phase and much larger airfoil velocities (outside the capabilities of the present experimental facility) would be needed to reach breakup onset. On the other hand, droplets whose diameter is larger than about 1500 µm tend to oscillate in shape and present deformations right after they leave the monodisperse droplet generator. So, they are not convenient if a reasonable repeatability is expected for the experiments. Incidentally, this issue of self-sustained shape oscillations of free-falling droplets, that represents an experimental limitation in the present study, has been studied in depth by Balla

et al [19] and Agrawal et al [20]. Summarizing, these are the two reasons why selected droplet diameters were in the range from 500 µm up to 1500 µm.

Regarding modelling aspects, it will be shown later, see equation (11), that a distinct parameter governs the droplet deformation equations. This parameter is the air density to droplet density ratio that, as it will be discussed, exerts a critical influence on the whole process. Then, the selection of ethyl-alcohol (density equal to 789 Kg/m^3) allows for a simple way to study the effect of the density ratio parameter. Furthermore, the smaller surface tension of alcohol (as compared to water) guarantees larger deformations that can be recorded accurately by the optical systems used in the experimental facility.

3.2. Cases #1, #2, #3, and #4

In these cases, the droplets deformed as oblate spheroids but they impinged the incoming airfoil before breakup. Fig. 5 presents the time sequence of deformation for case #4.
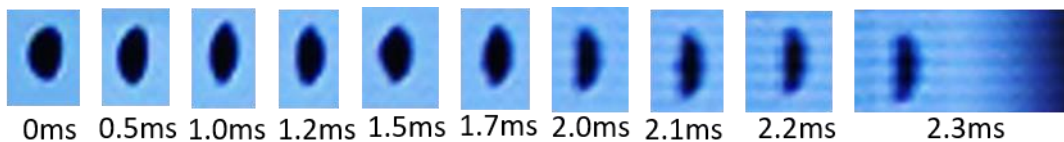
Figure 5. Time sequence of droplet deformation for case #4.

3.3. Case #5

The droplets deformed and went beyond the onset of breakup without actually fully breaking. The time sequence presented in fig. 6 illustrates the process (the flow goes from right to left). First, droplets deformed as oblate spheroids (0 ms to 4.6 ms) until a bulge (the bag) appeared in the surface facing the incoming flow (4.8 ms). The bulge increased significantly (5 ms to 5.2 ms) in a way that is representative of the bag-and stamen breakup mechanism (see, for example, fig.5 of ref. [15]). However, in this case, the airfoil (the dark shadow that is present in the right hand side of the frame corresponding to 5.2 ms) touched the droplet before the stamen in the bag-and-stamen breakup mechanism fully developed.
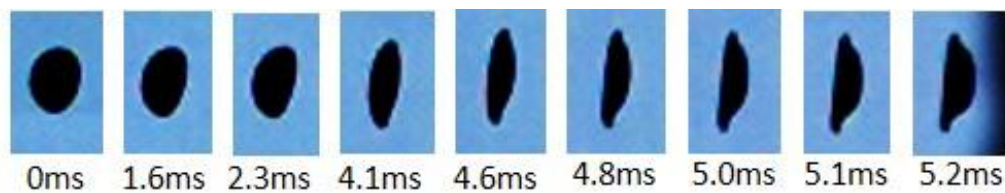
Figure 6. Temporal sequence of droplet deformation and breakup onset for case #5. The number below each frame indicates its sequence order during the photographic exposition.

3.4. Case #6

This case is a relevant one, so instead of presenting the results in one droplet per frame basis, whole vertical photograph strips are shown in fig. 7 that include the evolution of the droplets streams. A single droplet has been identified (framed in red) and has been tracked along the trips. The sequence is described next. First,

droplets deform as oblate spheroids (0 ms to 3.3 ms). Second, a bulge (the bag) appears in the surface facing the flow and it grows as in a conventional bag-and-stamen mechanism (3.75 ms to 4.15ms). Third, instead of the stamen shape starting to develop, a transitional phase appears in which the droplet thickens in the stream-wise direction (4.3 ms to 4.38 ms). Fourth, the thickening in the rear part of the droplet develops in the shape of a cone. This cone has, initially, a base and a height whose lengths are roughly similar (4.44 ms to 4.55 ms). However, as time passes by, the cone grows thinner until a finger like shape is formed (4.64 ms). To the knowledge of the authors, this cone plus finger breakup mechanism has not been reported previously in the literature.
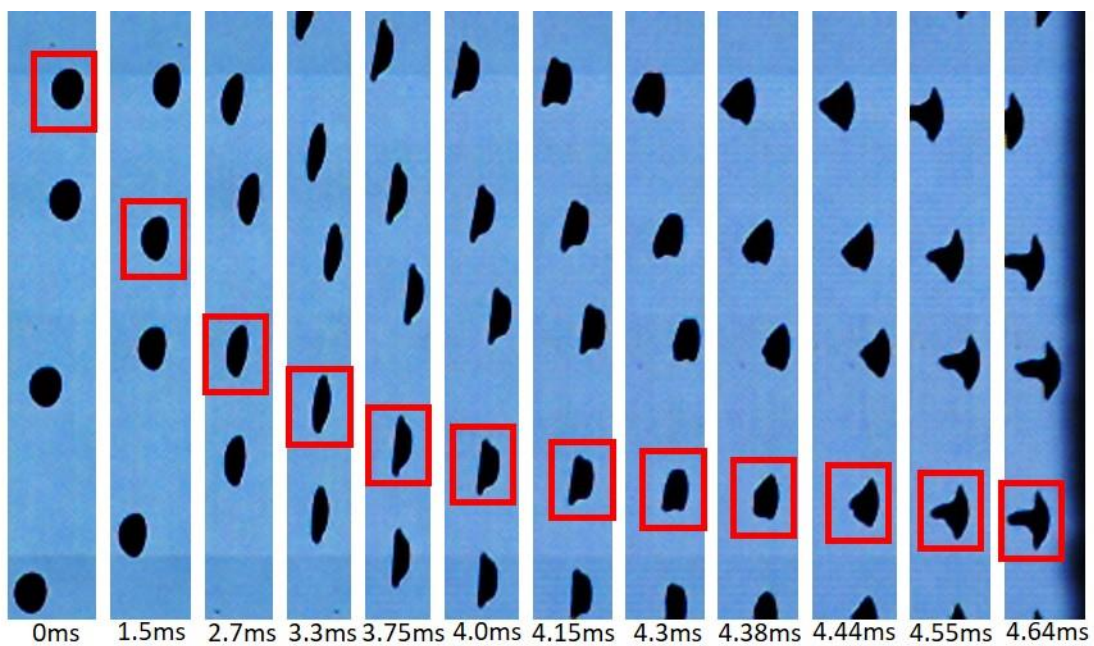
Figure 7. Time sequence of droplet deformation and breakup in case #6. Each frame contains between four and five droplets. The deformation and breakup sequence described in the text can be followed form left to right in the figure. A single droplet has been identified (framed in red) and has been tracked along the trips.

Next, fig. 8 expands the information contained in fig. 7 on a droplet per frame basis, and includes the results of the observations made by using the direct illumination technique described in section 2. The distance from the droplet to the airfoil, d, and the air velocity, U_{air}, are included for clarification purposes.
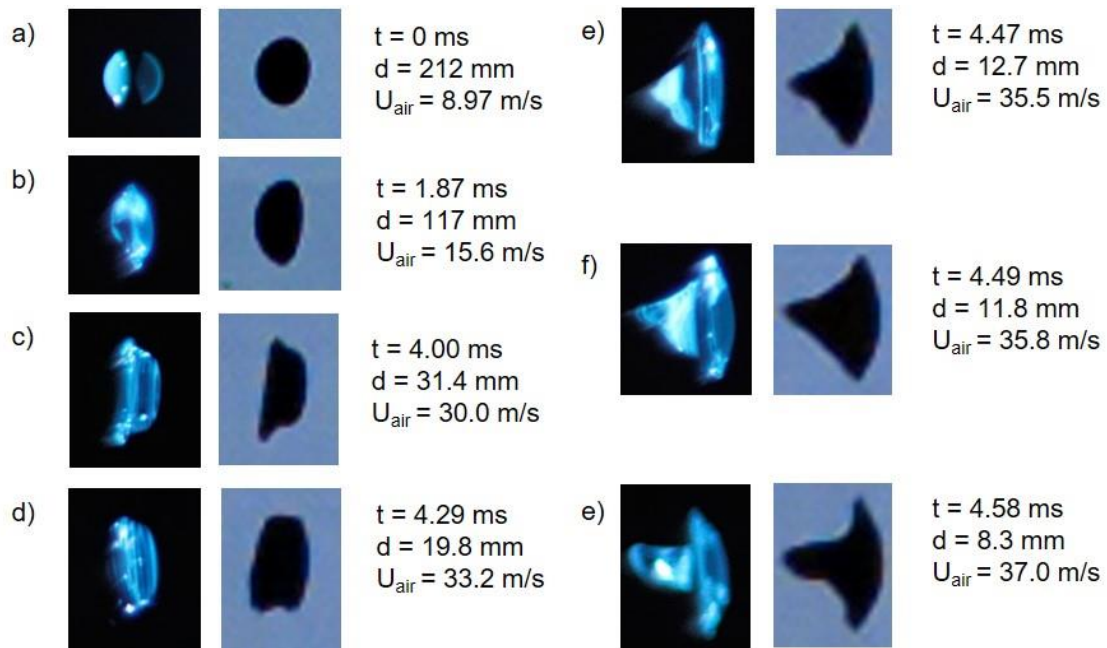

a) t = 0 ms
d = 212 mm
U_{air} = 8.97 m/s

b) t = 1.87 ms
d = 117 mm
U_{air} = 15.6 m/s

c) t = 4.00 ms
d = 31.4 mm
U_{air} = 30.0 m/s

d) t = 4.29 ms
d = 19.8 mm
U_{air} = 33.2 m/s

e) t = 4.47 ms
d = 12.7 mm
U_{air} = 35.5 m/s

f) t = 4.49 ms
d = 11.8 mm
U_{air} = 35.8 m/s

e) t = 4.58 ms
d = 8.3 mm
U_{air} = 37.0 m/s

Figure 8. Close-up view of a single droplet evolution, case #6, using the two different illumination systems described in the text.

The detailed sequence of the breakup mechanism, starting when the bulge appears and finishing when the finger-like rear structure is formed, is described more smoothly in time in fig. 9 where 25 frames are used for illustration purposes. The dark shadow that appears beyond the frame at 4.467 ms is the approaching airfoil.
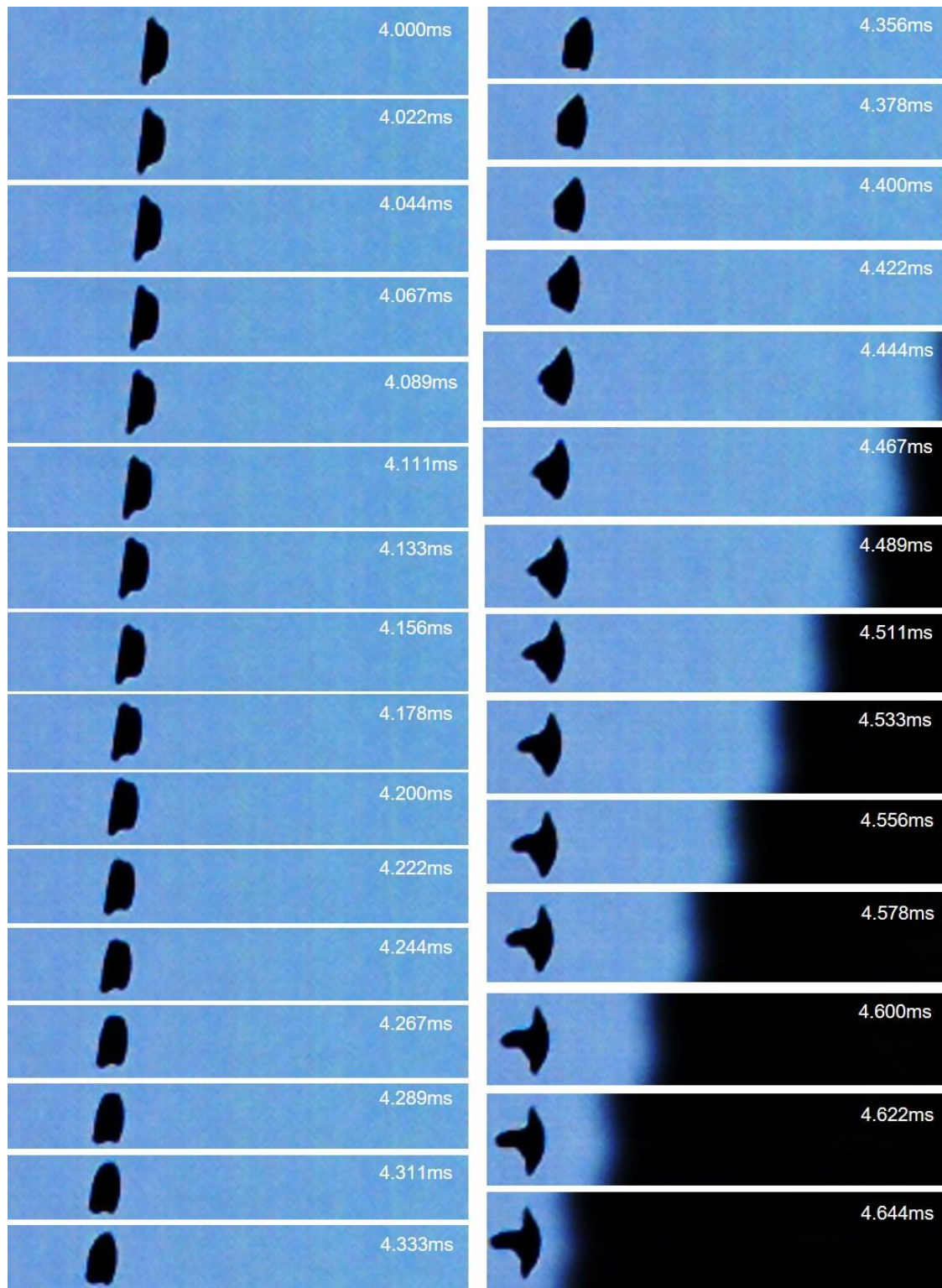
Figure 9. Full time sequence from breakup onset to fully developed breakup in case #6. The time sequence reads top-to-bottom, left to right. The black shadow that appears beyond 4.467 ms is the incoming airfoil.

A higher resolution expanded view of the cone-like shape is presented in fig. 10. The grey colour scale has been chosen so that some information about the three-dimensionality of the topology could be inferred from the picture. The flow-facing part of the droplet retains the oblate spheroid shape of the deformation phase (A). In the back, the cone is clearly observed (B). It is to be noted that its base diameter and its height have, basically, the same length. Regarding the transition between both parts, two different aspects could be pointed out. First, there appears to be a thin cylindrical section that connects both parts (C). This could be observed following the contour of the spheroidal shape: when it reaches its maximum diameter, it flattens and changes the shape derivative in the flow direction. Second, assuming that the cylindrical connecting part is indeed there, it seems that the cone generatrix and the surface of the cylindrical part span a finite angle larger than $\pi/2$ (D). This discontinuity in the shape derivative should disappear at the local level (at the junction). However, at the global level, it might suggest that, from a modelling point of view, governing flow equations inside the breaking droplet might behave quite differently in the forward and backwards regions.
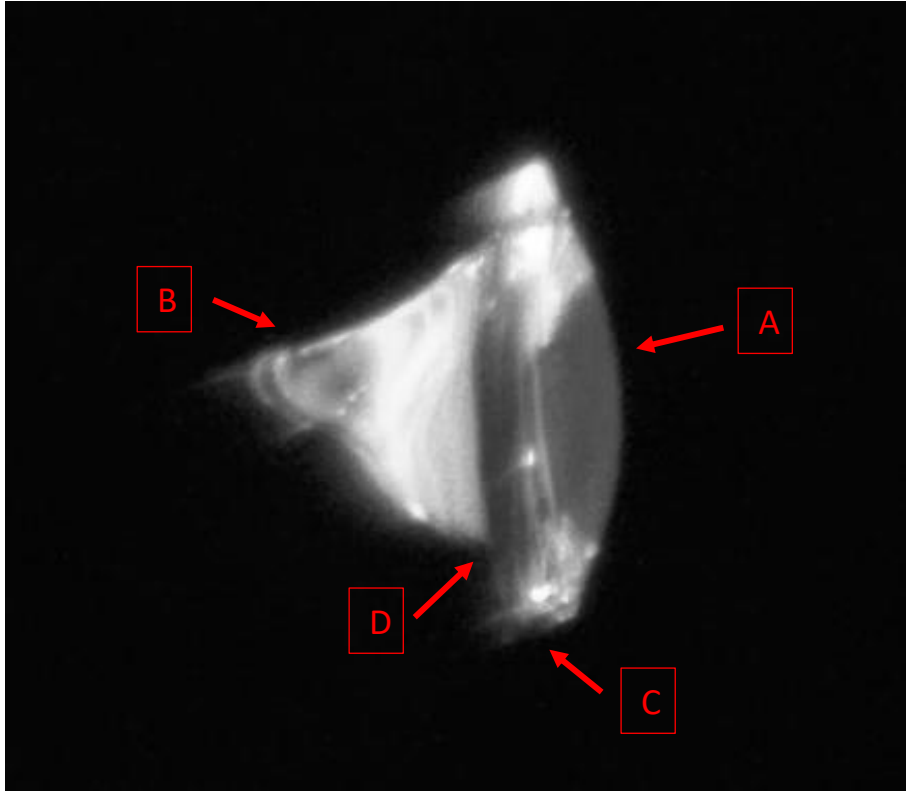
Figure 10. High resolution grey scale picture of the cone-like shape of the breaking droplet. Features marked A, B, C, and D are described in the text.

3.5. Cases #7 and #8

In the previous case #6, the droplet impinged the airfoil right after the finger-like rear structure was formed (see fig. 9). In these cases #7 and #8, ulterior evolution could be observed. In particular, see fig. 11 that corresponds to case #7, the front part of the droplet undergoes a large deformation and engulfs the back finger-like structure.
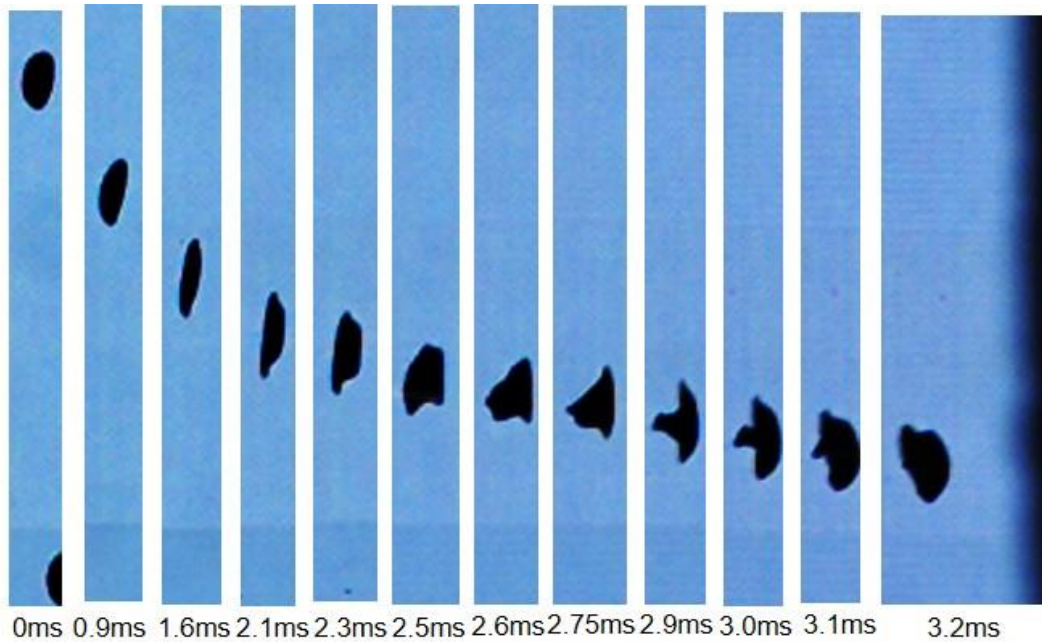
Figure 11. Time sequence (from left to right) of droplet deformation and
breakup in case #7.

3.6. Cases #9, #10, #11, and #12

These cases considered the larger droplets with diameters of about 1500 μm. Basically, their breakup behaviour was characterised by the absence of the finger-like topology and the presence, possibly caused by their large size, of shape asymmetries. Besides these asymmetries, the breakup mechanism appeared to revert back to a type of bag-and-stamen mode. Fig. 12 presents the time evolution of case #10. A close-up view of some representative frames of fig. 12 is presented in fig. 13.
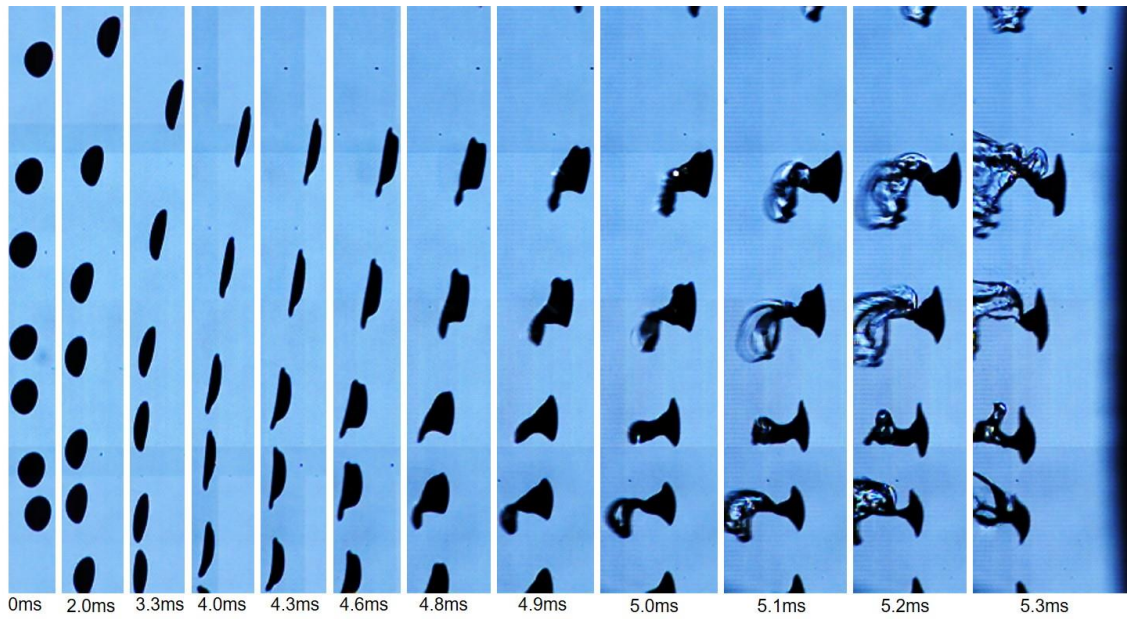
Figure 12. Time sequence (from left to right) of droplet deformation and breakup in case #10. Each frame contains between four and seven droplets.
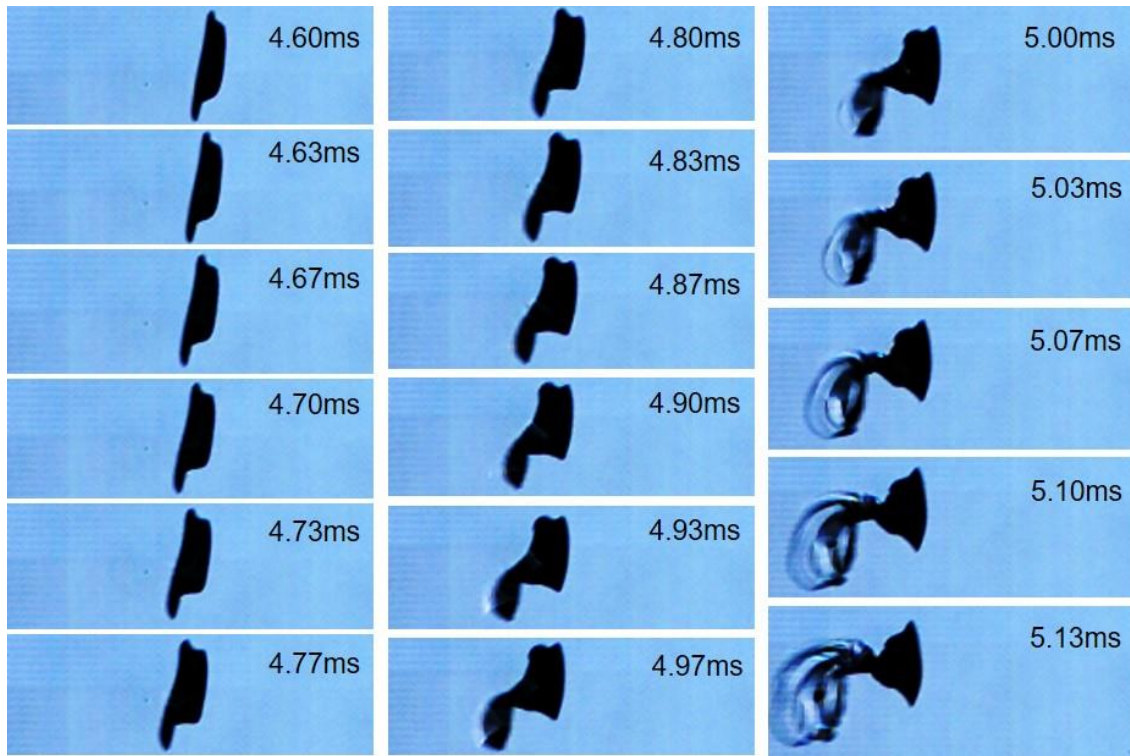
Figure 13. Close up view of representative time frames of figure 12 (case #10). The time sequence reads top-to-bottom, left-to-right.

4. Discussion

Droplet deformation and breakup phases are governed by different phenomena and should be treated differently. For example, the droplet deformation phase that involves fluids like water is not, normally affected, by viscous effects, Sor et al. [16]. However, after the onset of breakup, the Fluid Mechanics of the droplet internal flow starts to play a critical role that governs the breakup mechanism itself, Strotos et al. [13]. On the other hand, the growth of the surface droplet instabilities that lead to the ensuing breakup mechanism is governed by the acceleration (during the deformation phase) of the liquid phase into the gas phase, Joseph et al. [21].

So, in a sense, the deformation phase (that follows a certain set of equations) provides the initial conditions for the breakup phase (that follows a different set of equations). In this context, a simplified model for the deformation phase, based on the developments described by Sor et al [16] and Lopez-Gavilan et al [17], has been formulated and it is described below. The importance of modelling is to be stressed at this point because it may provide (even if the model is simplified) a guide for the understanding of the experimental results in this problem that involves so many parameters.

The problem under consideration is the 1D unsteady air flow past a deformable moving liquid droplet, see fig.14.
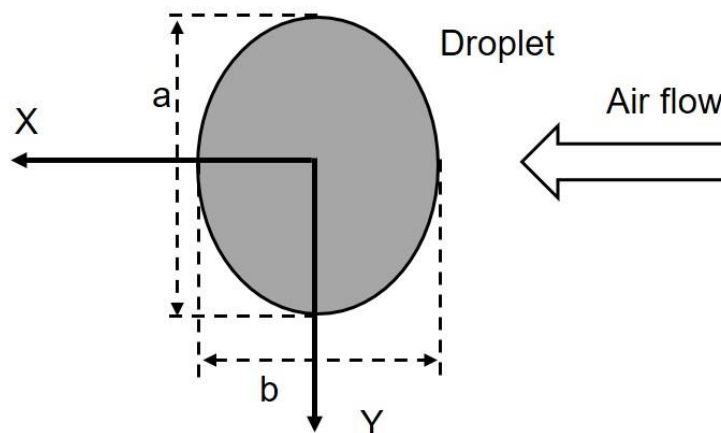

Figure 14. Sketch of the problem under consideration.

The model hypotheses are as follows:

- Dynamics effects associated to the vertical motion of the droplet (the direction of gravity) are neglected as compared to dynamics effects associated to the horizontal motion of the droplet (the direction of the

incoming air flow). This means that the problem is governed by two equations only: the droplet equation of motion in the horizontal direction, and the droplet deformation equation.

- Air velocity is much larger than droplet velocity (this because of the very large difference in densities), so the slip velocity (air velocity minus droplet velocity) can be approximated by the air velocity.

- Liquid phase viscous effects during the deformation phase are negligible as compared to surface tension and aerodynamics loading effects.

- The initial spherical droplet is assumed to deform as an oblate spheroid.

- The time dependent velocity of the incoming flow can be described by a certain number of parameters. For the problem under consideration, it is assumed that this flow is described by two parameters only. This is typical of the potential flow generated by a moving blunt object (for instance, the leading edge of an airfoil)

- The problem has one characteristic length: the initial droplet radius. However, it does not have a characteristic time. This allows for the selection of the reference time used to render variables dimensionless with the only criterion of writing the model equations with a minimum number of governing parameters. Note that a possible reference time, the droplet radius divided by a characteristic velocity of the incoming flow, is the

residence time of a fluid particle around the droplet, not the characteristic time of droplet motion.

Model equations (1-2) and boundary conditions (3-4), see ref. [16], are:

$$m_d \frac{d^2x}{dt^2} = \frac{1}{2}\rho_a U_s^2 \pi a^2 \left[\left(C_{D_{sphere}}^{\left(\frac{b}{a}\right)^3} \cdot C_{D_{disk}}^{1-\left(\frac{b}{a}\right)^3} + k\frac{b}{U_s^2}\frac{dU_s}{dt} \right) \right] \tag{1}$$

$$\frac{3}{16}m_d \frac{d^2a}{dt^2} = -\frac{4}{3}\sigma\frac{dA_s}{da} + \frac{1}{2}C_P \rho_a U_s^2 \pi R_d^2 \tag{2}$$

$$x(0) = \left(\frac{dx}{dt}\right)_{t=0} = 0 \tag{3}$$

$$a(0) = R_d \,, \left(\frac{da}{dt}\right)_{t=0} = 0 \tag{4}$$

In equation (1), m_d, x, t, and ρ_a are droplet mass, horizontal coordinate, time coordinate and air density respectively. U_s is the time dependent slip velocity (air minus droplet velocity) that is taken as the air velocity. a and b are the maximum and minimum radiuses of the oblate spheroid, see figure 14, that represents the droplet during the deformation phase. They are related by the fact that the volume of the initial sphere and that of the subsequent spheroids is the same. This

translates into the relation $R_d^3 = a^2 b$. From the physics point of view, equation (1) is the dynamics equation of motion of the droplet. The left hand-side terms is the droplet mass times its acceleration. The right hand-side represents the drag force on the droplet caused by the incoming flow. Following ref. [16] the drag is modelled by the addition of a steady plus an unsteady term. The steady term is obtained by interpolating between the steady drag of a sphere, $C_{D_{sphere}}$, and a disk, $C_{D_{disk}}$, that depend on the ratio b/a. They were modelled as: $C_{D_{sphere}} = (24/Re) + (6/(1 + Re^{0.5})) + 0.4$, see White [22], and $C_{D_{disk}} = 1.17$. Where Re is the instantaneous Reynolds number. The unsteady term depends on dU_s/dt, on b, and on a calibration coefficient, k, whose value, equal to 9, was found to be nearly constant over a very wide parametric range [14]. That is, the information on the flow unsteadiness enters the equation of motion via the time derivative of the incoming air flow.

Regarding equation (2), m_d, σ, A_s, and C_P are droplet mass and surface tension, surface area of the oblate spheroid, and pressure coefficient (taken to be 0.93) respectively. From the physics standpoint, equation (2) represents the deformation of a mass-spring system subjected to a deforming aerodynamics force (the second term in the right hand-side of equation (2)) and a surface tension based restoring force (the first term in the right hand-side of equation (2) that acts as the "spring"), see [16]. The deforming force is related to the instantaneous aerodynamics loading that depends functionally on U_s^2. The restoring force depends on the surface tension parameter σ, and, also, on how

much the droplet surface area varies with regard to changes in the droplet diameter, dA_s/da .

If the 1-D unsteady flow is generated by an approaching blunt body (say a circular cylinder of radius R_c), U_s, as seen in the droplet reference frame, is given by:

$$U_s = U_m \frac{R_c^2}{(R_c + r)^2}$$

(5)

Where U_m is the velocity of the incoming cylinder, R_c is its radius, and r is the distance from the droplet to the leading edge of the cylinder. Then, $r = r_0 - U_m t$ where r_0 is the initial distance (at $t = 0$) between droplet and cylinder. To start the integration of equations (1-2), r_0 is taken as $r_0 = \beta R_c$ where $\beta \gg 1$ (formally, r_0 should be infinite). If, for example, $\beta = 9$ then $U_s = 0.01\, U_m$ at $t = 0$. Note that this finite initial velocity is required to start the numerical integration of equations (1-2) without numerical instabilities. In the experimental tests, the maximum droplets radiuses, R_d, were about 0.75 mm, while the airfoil leading edge radius, R_c, was 157 mm. Then, $R_c \gg R_d$ so relation (5) could be taken as a reasonable approximation to the air flow velocity past the droplet. Furthermore, exponent 2 in relation (5) is valid for a circular cylinder only. In the case of the experiments, PIV was used to characterize the flow field generated by the blunt airfoil, and it was found that the flow in the stagnation line followed a

law similar to that of relation (5) but with a different n exponent: $n = 1.75$. Then, summarizing, the slip velocity U_s was taken as:

$$U_s = U_m \frac{R_c^n}{[(1 + \beta)R_c - U_m t]^n} \tag{6}$$

Finally, the surface area, A_s, of the oblate spheroid is:

$$A_s = 2\pi a^2 + \pi \frac{b^2}{e} \ln\left(\frac{1 + e}{1 - e}\right), \qquad e = \left(1 - \frac{b^2}{a^2}\right)^{\frac{1}{2}} \tag{7}$$

Now, to render equations (1-2) and boundary condition (3-4) dimensionless, the following variables were defined:

$$\eta = \frac{x}{R_d}, \alpha = \frac{a}{R_d}, \tau = \frac{t}{t_{ref}}, \qquad t_{ref} = \left(\frac{3\pi}{16} \frac{\rho_d R_d^3}{\sigma}\right)^{\frac{1}{2}} \tag{8}$$

Also:

$$\mathbb{U}_s = \frac{U_s t_{ref}}{R_d}, \qquad \mathbb{U}_m = \frac{U_m t_{ref}}{R_d}, \qquad \mathbb{A}_s = \frac{A_s}{R_d^2} \tag{9}$$

Then, the dimensionless equations and boundary conditions of the problem are:

$$\frac{8}{3\lambda}\frac{d^2\eta}{dt^2} = \mathbb{U}_s^2 \, \alpha^2 \, C_{D_{sphere}}^{1/\alpha^3} \, C_{D_{disk}}^{1-1/\alpha^3} + k\frac{d\mathbb{U}_s}{d\tau} \qquad (10)$$

$$\frac{d^2\alpha}{dt^2} = -\frac{d\mathbb{A}_s}{d\alpha} + 2\lambda \, C_p \, \mathbb{U}_s^2 \qquad (11)$$

$$\eta(0) = \left(\frac{d\eta}{d\tau}\right)_{\tau=0} = 0 \qquad (12)$$

$$\alpha(0) = 1 \, , \left(\frac{d\alpha}{d\tau}\right)_{\tau=0} = 0 \qquad (13)$$

Where $\lambda = \rho_a/\rho_d$ is the density ratio parameter. The onset of breakup, [17], is defined as the moment when the wavelength of the droplet surface disturbance equals the hydraulic diameter of the droplet. Note that this instability mode is assumed to be the classical one associated the case of a high density fluid accelerating into another fluid with a much lower density. In practical terms, this criterion for the onset breakup, [17], can be expressed as a relation between the surface area of the deforming droplet and its acceleration as follows:

$$\frac{64}{3\pi}\frac{1}{\mathbb{A}_s}\left(\frac{d^2\eta}{d\tau^2}\right)^{\frac{1}{2}} = 1 \qquad (14)$$

Equations (10-11) and boundary conditions (12-13) have been solved for the parameters involved in case #6. To allow for a better comparison, the idealized boundary conditions (12-13) were modified to account for the actual measured data at $t = 0$. That is, instead of imposing $\alpha(0) = 1$, the actual experimental value of α as the droplet entered the field of view of the recording camera was prescribed: $\alpha(0) = 1.052$. Also, measured initial droplet position and velocity were used as initial conditions: $\eta(0) = 0.015$ and $(d\eta/d\tau)_{\tau=0} = 1.473$. This is important because the monosized droplet generator does not necessarily ensures that the droplets fall strictly in the vertical direction. It was found that, sometimes, they start with a finite horizontal velocity component. Figures 15 and 16 present the comparison between the measured and computed values of the droplet radius and displacement as a function of time. The larger square boxes mark the onset of breakup. The issue of uncertainty and repeatability of the measured data is addressed in the Annex.
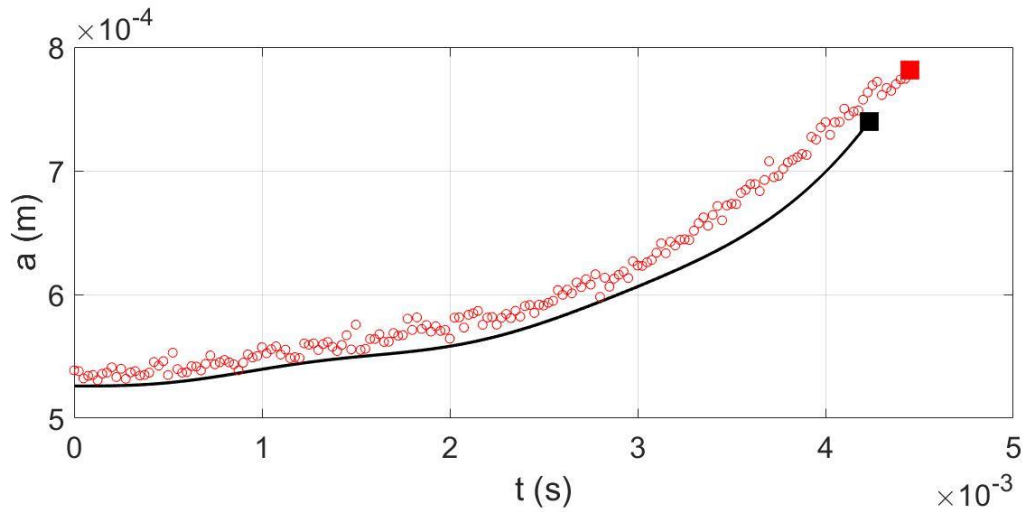
Figure 15. Case #6. Comparison between the measured (red dots) and computed (solid black line) values of the maximum radius, a, of the deforming droplet as a function of time. The larger squares mark the onset of breakup.
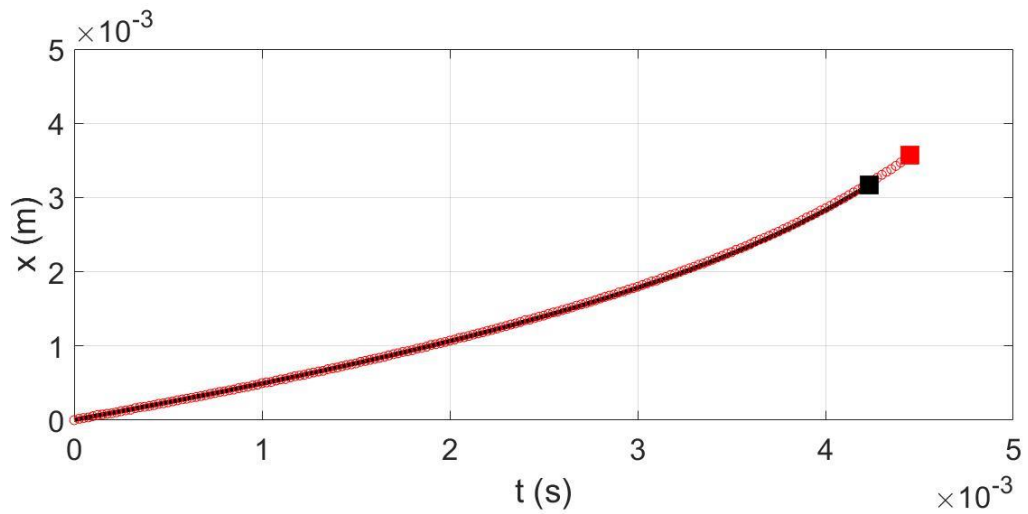

Figure 16. Counterpart of figure 15 for the horizontal displacement, x , of the droplet

The conclusion is that the model predicts reasonably the time evolution of both droplet deformation and position. The experimental uncertainty when measuring a is larger than when measuring x . The reason is that the centroid of the droplet can be tracked more accurately than its outer boundary (the spatial measurement resolution is the size of the pixel).

Now, the model results of case #6 (alcohol) are compared to a similar case (tagged as case #6-b) in which all geometry and air velocity parameters are the same except that the droplet fluid is water. Plots of droplet deformation, position, velocity and acceleration are presented in figures 17 to 20 respectively. It has been preferred to carry out this comparison using dimensional variables. The reason is that dimensionless parameters that govern the deformation phase are different from those that govern the breakup stage. Then, a discussion based on the dimensionless deformation phase parameters may not be strictly appropriate.
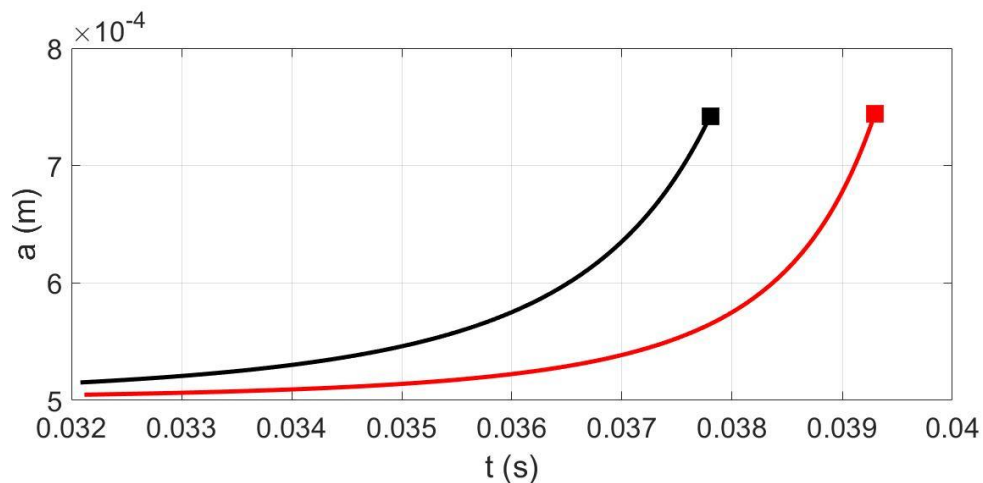

Figure 17. Comparison between time evolution of droplet deformation for cases #6 (alcohol, black line) and #6-b (water, red line). The squares mark the instant of onset breakup.
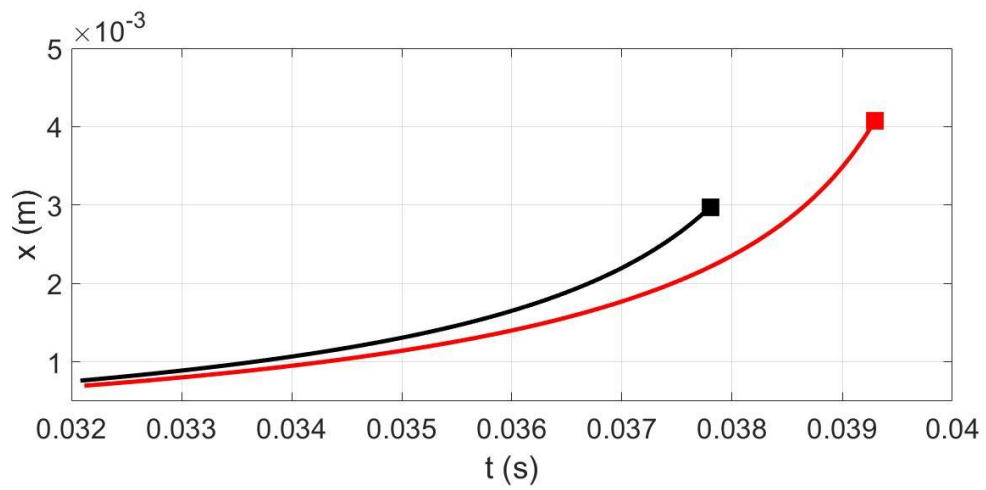
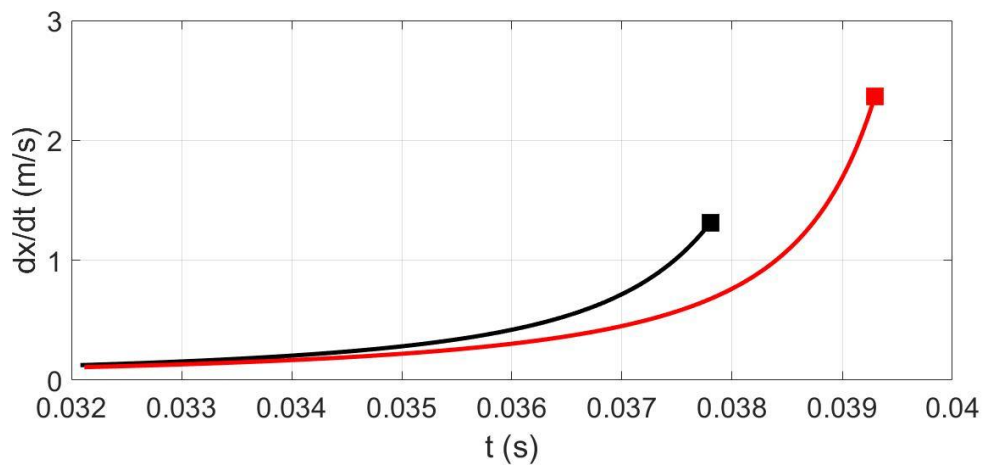Figure 18. Counterpart of fig. 17 for the horizontal position of the droplets.

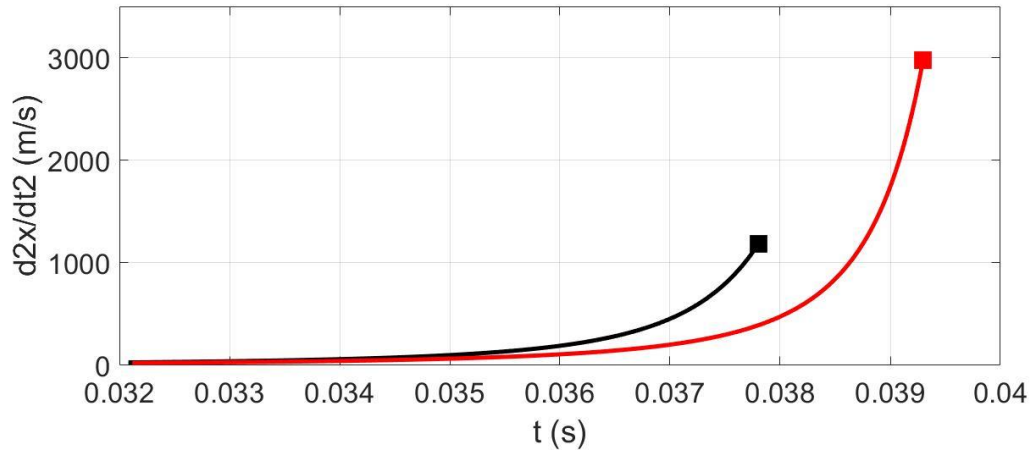Figure 19. Counterpart of fig. 17 for the horizontal velocity of the droplets.

Figure 20. Counterpart of fig. 17 for the horizontal acceleration of the droplets.

Regarding fig. 17, it could be observed that that in both cases #6 and #6-b, droplets reach the onset of breakup when their deformation (the a parameter, see fig. 14) is nearly the same. However, in the case of alcohol, this deformation is reached earlier than in the case of water. When the alcohol droplet reaches the onset of breakup stage, its maximum radius is about 0.00075 m while, at that instant, the water radius is 0.00055 m (about one third smaller). The fact that alcohol droplets deform faster than similar water droplets could be caused by the fact that they have a smaller (by a factor of the order of 3) surface tension. Also, it is important to note that the alcohol droplet reaches the onset of breakup when the incoming air velocity is 23 m/s while the water droplet starts breaking when the air velocity reaches 40 m/s. Then, regarding droplet motion dynamics, three factors should be accounted for: a) the alcohol droplet smaller surface tension causes larger deformations that increase drag and, therefore, increase the pressure force that propels the droplet forwards, b) the alcohol droplet smaller density also contributes to increase its velocity and acceleration along the x axis,

and c) the proposed unsteady drag model depends on the air acceleration, so the larger the acceleration the larger the drag force. These effects are apparent in figs. 19 and 20 where it could be observed that, for the same time, the velocity and acceleration of alcohol droplets are significantly larger than those of water droplets. On the other hand, it is also worth noting that the water droplet requires far larger accelerations than the alcohol droplet to reach the breakup onset. Specifically, it could be observed in fig. 20 that at breakup onset conditions (marked by the black and red squares), the water droplet has an acceleration that is nearly three times larger than that of the alcohol droplet. Re-writing equation (14) in dimensional variables:

$$\frac{16}{(3\pi)^{1/2}}\frac{R_d^3}{A_s}\left(\frac{\rho_d}{\sigma}\frac{d^2x}{dt^2}\right)^{\frac{1}{2}} = 1 \tag{15}$$

Then, if deformation at breakup onset is about the same and the initial droplet radius is the same, equation (15) implies:

$$\left(\frac{\rho_d}{\sigma}\frac{d^2x}{dt^2}\right)_{fluid} \cong constant \tag{16}$$

That can be translated into:

$$\left(\frac{\rho_d}{\sigma}\frac{d^2x}{dt^2}\right)_{alcohol\ droplet} \cong \left(\frac{\rho_d}{\sigma}\frac{d^2x}{dt^2}\right)_{water\ droplet} \tag{17}$$

So, given the actual values of alcohol and water density and surface tension respectively, it could be found from relation (17) that the water droplet requires, to reach breakup onset, an acceleration about three times larger than the alcohol droplet. Possibly, this significantly larger acceleration has an important effect on the flow topology inside the droplet, so this might be one of the reasons for the appearance of two different breakup modes: "bag and stamen" and "cone" respectively. It is, nevertheless, important to stress that this discussion refers, only, to the conditions of the breakup onset, not to the breakup phase itself. For this purpose, another model, that is out of the scope of the present study, would be needed.

5. Conclusions

An experimental study has been carried out on the problem of aero-breakup mechanisms associated to unsteady loading. The study was performed in a rotating arm facility and the working fluid was ethyl-alcohol. The idea was to use a fluid less dense than water (789 kg/m^3 versus 1000 kg/m^3) and whose surface tension is, also, significantly smaller (0.023 N/m versus 0.073 N/m). In this way, it was possible to explore a range of governing parameters that where not addressed in previous studies. The unsteady flow (as seen from the droplet reference frame) was generated by an approaching airfoil whose velocity varied in the range form 30 m/s up to 60 m/s.

The main outcome of the study has been the identification of a new droplet breakup mechanism characterized by the presence of a large cone-like structure

in the downstream side of the droplet. The formation sequence is as follows: a) the droplet starts to deform as an oblate spheroid; b) a bulge appears in the surface facing the flow; c) a transitional phase appears in which the droplet thickens in the stream-wise direction; d) the thickening in the rear part of the droplet develops in the shape of a cone that has, initially, a base and a height whose lengths are roughly similar; e) the cone grows thinner until a finger like shape is formed. To the knowledge of the authors, this cone plus finger breakup mechanism has not been reported previously in the literature. The new mechanism was identified in droplets having a diameter of the order of 1000 μm. Smaller droplets ($\sim$ 500 μm), dominated by the restoring surface tension force, did not actually break. Larger droplets ($\sim$ 1500 μm) presented large asymmetries with no clear breakup pattern.

Based on a deformation and breakup onset model developed by the authors, a comparison was carried out between the deformation phase of ethyl-alcohol and water droplets of the same size under the same loading conditions. The model predicts deformation, position, velocity, and acceleration of the droplet up to the onset of breakup; i.e. the model does not predict phenomena in the subsequent breakup phase. Then, this comparison addressed the initial conditions of the breakup phase, not the breakup phase itself. It was found that, for the same time instant, ethyl-alcohol droplets presented larger deformation, velocity, and acceleration that their water counterparts. The reason could be that smaller surface tension implies larger deformations and, therefore, larger drag force that tends to propel the droplet faster. Also, smaller density favours these larger velocity and acceleration. The conclusion is that this larger acceleration changes

significantly the flow topology inside the droplet and leads to a different breakup mechanism.

Acknowledgements

References

[1] M. Pilch, C.A. Erdman, Use of breakup time data and velocity history data to predict the maximum size of stable fragments for acceleration-induced breakup of a liquid drop, Int. J. Multiphase Flow, 13(6) (1987) 741-757.

[2] D. R. Guildenbecher, C. Lopez-Rivera, P. E. Sojka, Secondary atomization, Exp. Fluids 46 (2009) 371–402.

[3] T.G. Thoeofanous, Aerobreakup of Newtonian and viscoelastic liquids, Annu. Rev. Fluid Mech. 43 (2011) 661–90.

[4] R. Krechetnicov, Rayleigh–Taylor and Richtmyer–Meshkov instabilities of flat and curved interfaces, J. Fluid Mech. 625 (2009) 387–410.

[5] D. Chaitanya, S. Basu, Phenomenology of disruptive breakup mechanism of a levitated evaporating emulsion droplet, Exp. Therm. Fluid. Sci., 115 (2020) 110086.

[6] M. Ashar, D. Arlov, F. Carlsson, F. Innings, R. Andersson, Single droplet breakup in a rotor-stator mixer, Chem. Eng. Sci. 181 (2018) 186–198.

[7] M.V. Piskunov, P.A. Strizhak, Using Planar Laser Induced Fluorescence to explain the mechanism of heterogeneous water droplet boiling and explosive breakup, Exp. Therm. Fluid. Sci., 91 (2018) 103–116.

[8] S. Kumar, P. Kumar, P. Kolhe, K. Chandra, Deformation and breakup of droplets in an oblique continuous air stream, Int. J. Multiphase Flow, 122 (2020) 103141.

[9] H. Zhao, H-F. Liu, J-L. Xu, W-F. Li, Secondary breakup of coal water slurry drops, Phys. Fluids, 23 (2011) 113101.

[10] A.V. Minakova, A.A. Shebelevaa, P.A. Strizhakc, M.Yu. Chernetskiyb, R.S. Volkovc, Study of the Weber number impact on secondary breakup of droplets of coal water slurries containing petrochemicals, Fuel 254 (2019) 115606.

[11] D. Pan, Q. Chen, Y. Zeng, B. Li, Droplets containing large solid particle inside formation and breakup dynamics in a flow-focusing microfluidic device, Exp. Therm. Fluid. Sci. 115 (2020) 110103.

[12] S. K. Soni, P. K. Kirar, P. Kolhe and K. C. Sahu, Deformation and breakup of droplets in an oblique continuous air stream, Int. J. Multiphase Flow, 122, (2020), 103141.

[13] G. Strotos, I. Malgarinos, N. Nikolopoulos, M. Gavaises, Predicting droplet deformation and breakup for moderate Weber numbers, Int. J. Multiphase Flow, 85 (2016) 96–109.

[14] A. García-Magariño, S. Sor, A. Velazquez, Experimental characterization of water droplet deformation and breakup in the vicinity of a moving airfoil, Aerosp. Sci. Technol. 45 (2015) 490–500

[15] A. García-Magariño, S. Sor, A. Velazquez, Data reduction method for droplet deformation experiments based on High Order Singular Value Decomposition, Exp. Therm. Fluid. Sci, 79 (2016) 13–24

[16] S. Sor, A. García-Magariño, A. Velazquez, Model to predict water droplet trajectories in the flow past an airfoil, Aerosp. Sci. Technol. 58 (2016) 26–35.

[17] P. Lopez-Gavilan, A. Velazquez, A. García-Magariño, S. Sor, Breakup criterion for droplets exposed to the unsteady flow generated by an incoming aerodynamic surface, Aerosp. Sci. Technol. 98 (2020) 105687.

[18] B. Veras-Alba, J. Palacios, M. Vargas, C. Ruggeri, T.P. Bartkus, Experimental Investigation of Supercooled Water Droplet Breakup near Leading Edge of Airfoil, J. Aircraft, 55 (2018) 1970-1984.

[19] M. Balla, M. T. Tripathi, K. C. Sahu, Shape oscillations of a nonspherical water droplet, Phys. Rev. E, 99, (2019) 023107.

[20] M. Agrawal, A. R. Premlata, M. K. Tripathi, B. Karri, K. C. Sahu, Nonspherical liquid droplet falling in air, Phys. Rev. E, 95 (2017) 033111.

[21] D.D. Joseph, J. Belanger, G. S. Beavers, Breakup of a liquid drop suddenly exposed to a high-speed airstream, Int. J. Multiphase Flow 25 (6-7) (1999) 1263-1303.

[22] F. M. White, Viscous Fluid Flow, McGraw Hill, (2006), New York.

Annex 1

This Annex is concerned with the uncertainty and repeatability of the measured data. In particular, for the sake of brevity, only the measured deformation of the droplet will be considered. This is because, as it could be observed in figs. 14

and 15, tracking of the droplet deformation shows larger uncertainty that droplet position. Fig. A1 presents the dimensionless droplet deformation versus dimensionless time associated to case #6 (see figs. 14 and 15). The discrete deformation data (black line) has been fitted with a third order polynomial (the red solid line in fig. A1). The uncertainty band (the band where all measurements lay) has been plotted in the shape of two broken red lines. It has been found that $\alpha_i \in \bar{\alpha} \pm 0.03$, where α_i stands for any measurement and $\bar{\alpha}$ is the average deformation (the red solid line).
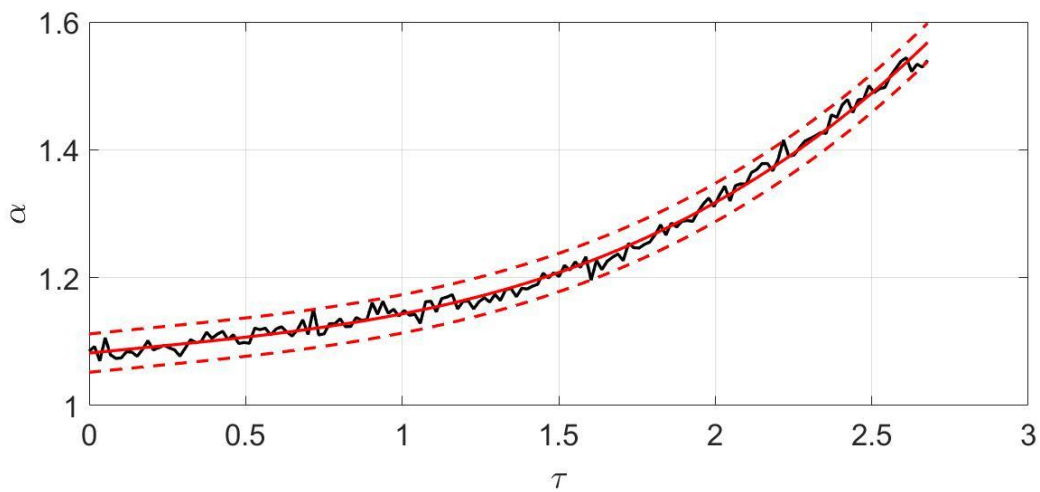

Figure A1. Droplet deformation, α, uncertainty band of case #6. Discrete measured data: solid black line; average data: solid red line; uncertainty band: broken red lines.

Next, three cases have been considered: case #6 ($R_d = 0.00047\ m$, black solid line in fig. A2), case #6c ($R_d = 0.00049\ m$, blue solid line), and case #6d ($R_d = 0.00048\ m$, red solid line). Fig. A2 presents the discrete data associated to the three cases as well as their third order polynomial fitting. If the repeatability

index is defined as $\left(max\left|\alpha_{i,max}, \alpha_{i,min}\right| - 1\right)/(\bar{\alpha} - 1)$, it is found that its value is of the order of 3% that is smaller than the measurement uncertainty. This means that the results are repeatable within the experimental uncertainty of the measurement system.
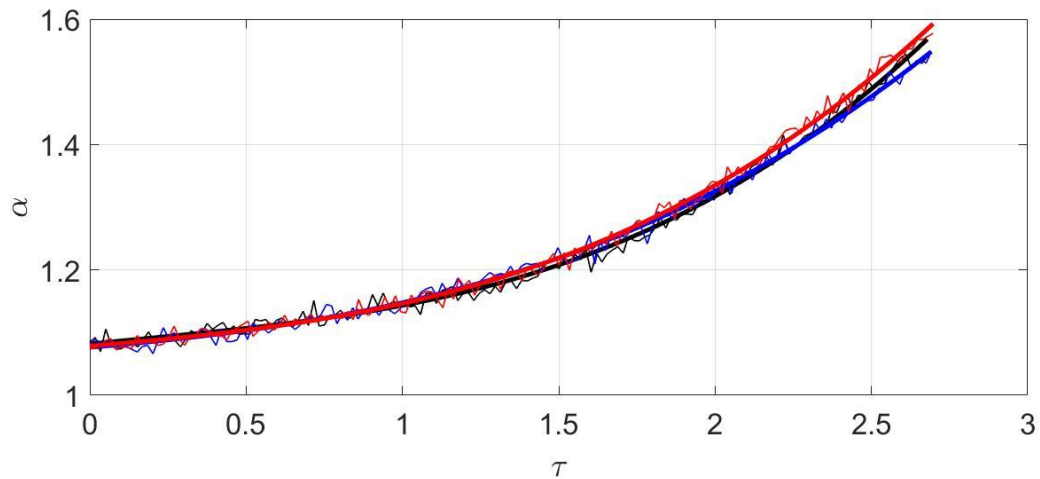

Figure A2. Repeatability of three cases with droplet radius around 0.0005 m. $R_d = 0.00047\ m$, black solid line, $R_d = 0.00049\ m$, blue solid line, and $R_d = 0.00048\ m$, red solid line. Third order polynomial fitting are plotted with the same colour codes.